Weather and Climate Extremes 41 (2023) 100587

Contents lists available at ScienceDirect

Weather and Climate Extremes

journal homepage: www.elsevier.com/locate/wace

Mechanisms of the transport height of water vapor by tropical cyclones on heavy rainfall

Tianao Liu [a], Yilun Chen [a], Shumin Chen [a], Weibiao Li [a], Aoqi Zhang [a,*]

[a] Southern Marine Science and Engineering Guangdong Laboratory (Zhuhai), School of Atmospheric Sciences, Sun Yat-sen University, Zhuhai, 519082, China

ARTICLE INFO

Keywords:
Heavy precipitation
Transport height of water vapor
Numerical models
Microphysical processes
Tropical cyclones

ABSTRACT

The moisture transport by tropical cyclones is characterized by high intensity and altitude, which may affect the microphysical processes of heavy rainfall triggered by tropical cyclones. In this study, we used the Weather Research and Forecasting (WRF) model to conduct numerical simulations on a heavy rainfall event near the Yangtze River Delta induced by Super Typhoon Mangkhut (2018). The vertical distribution of water vapor was modified to highlight the impact of moisture transport at various heights. The results showed that the distribution and intensity of the rainfall event changed with the transport height of water vapor. Ensuring that the water vapor content in the column kept constant, the total amount of precipitation in the region was greatest when the transport occurred primarily at low levels, and smallest when the transport occurred primarily at mid-levels. Detailed analysis of cloud water, rainwater, and frozen hydrometeors showed that liquid- (ice-) phase processes were the dominant microphysical processes when the transport height is low (mid-to-low). The deposition and riming processes contributed to heavy precipitation when the transport height was at the mid-to-upper levels. Our findings underscore the influence of moisture transport with high intensities and altitudes by tropical cyclones on microphysical processes, ultimately leading to changes in the distribution and intensity of heavy rainfall. Therefore, when analyzing heavy precipitation events, particular attention should be given to the moisture transport at the mid-to-upper levels.

1. Introduction

Adequate water vapor supply is crucial for the generation of heavy precipitation events. Therefore, analyzing the moisture transport during such events can provide valuable insights (Galarneau et al., 2010; Lavers and Villarini, 2015; Moore et al., 2013). The precipitation processes in the pre-summer rainy season in southern China, continuous Meiyu rainfall near the Yangtze River Basin, and heavy rainfall in northern China during mid-summer are all closely related to the moisture transport (Du and Chen, 2019; Wang et al., 2014; Wu et al., 2020; Zhang et al., 2020). In such precipitation events, particular attention is often given to low-level moisture transport, especially at 850 hPa. For instance, Zhang et al. (2020) suggested that the early morning peak of Meiyu rainfall in the Yangtze Plain during atypical Meiyu years was closely related to low-level water vapor flux. Du and Chen (2019) studied a heavy rainfall event in southern China and found that it was associated with a synoptic-system-related low-level jet and a boundary-layer jet, which transported warm moist air and favored moist convection.

Tropical cyclones are intense synoptic systems with strong moisture transport that can reach high altitudes. The low-level moisture transport is an important factor in the occurrence of remote heavy rainfall, which is away from the main body of tropical cyclones (Chen, 2006; Galarneau et al., 2010; Yu et al., 2020). An analysis of water vapor during severe rainstorms closely associated with Typhoons Tembin (2012) and Bolaven (2012) showed that the transport height of water vapor in the precipitation process was mainly below 700 hPa and that tropical cyclones interacted with the subtropical high; as the tropical cyclone moved northwest, the wind speed between the tropical cyclone and the subtropical high gradually increased, and a large amount of water vapor was transported to the precipitation area (Shan et al., 2014). During a heavy precipitation event in Beijing on July 21, 2012, the water vapor channel between Typhoon Vicente and the subtropical high played an important role; the stronger the typhoon, the greater the amount and area of precipitation (Wen et al., 2015). The analysis of a precipitation process in Japan in 2004 showed that the northward moisture transport by Typhoon Songda caused heavy rainfall and that, without this typhoon, the precipitation event would have been significantly weaker

* Corresponding author.
E-mail address: zhangaoq3@mail.sysu.edu.cn (A. Zhang).

https://doi.org/10.1016/j.wace.2023.100587
Received 5 December 2022; Received in revised form 13 June 2023; Accepted 13 June 2023
Available online 17 June 2023

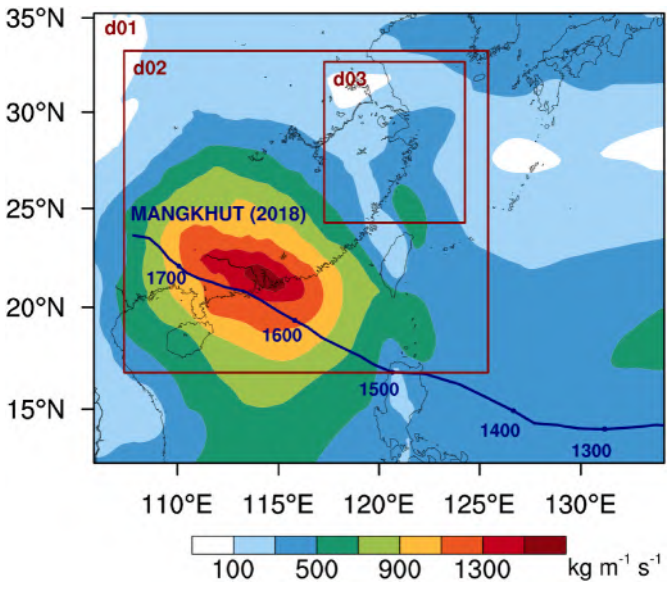

Fig. 1. Domains of the numerical trials. d01 represents the parental domain and d02 and d03 represent the two nested domains. The blue line is the path of Typhoon Mangkhut (2018). The numbers beside the path represent the time at which the center of the typhoon passed through that point—for example, 1300 represents 00:00Z on September 13, 2018. Distribution of average water vapor flux from September 16 to September 17, 2018 derived from ERA5 data is shown in filled contours. (For interpretation of the references to colour in this figure legend, the reader is referred to the Web version of this article.)

(Wang et al., 2009). These studies discussed moisture transport in the lower troposphere induced by tropical cyclones, mainly because the average mixing ratio of water vapor in mid-to-upper levels is much smaller than that at low levels (approximately 1:10) (Feltz et al., 2003; Gutnick, 1962).

However, with adequate water vapor and high intensity, tropical cyclones may reach the upper troposphere or even lower stratosphere and transport moisture to anomalous heights over both the surrounding and remote locations (Fu et al., 2013; Plotnik et al., 2021). Although moisture in the upper levels does not constitute a large proportion of the whole column, the effect of water vapor in upper levels in determining the Earth's outgoing longwave radiation is comparable to that of the lower troposphere (Lindzen, 1990; Shine and Sinha, 1991). Moreover, moisture in the upper levels promotes ice-phase processes, such as deposition and riming, affecting latent heat release, which may lead to ice particles generating, melting, and finally falling to the ground to intensify precipitation (Houze, 2012; Li et al., 2016; Niu et al., 2010; Rutledge and Hobbs, 1984; Zuo et al., 2022). Fu et al. (2003) analyzed two mesoscale heavy precipitation systems and showed that in stratiform precipitation, raindrops do not collide and coalesce below the freezing layer, whereas raindrops in convective precipitation coalesce; evaporation, break-up, and other processes may also occur. Chen et al. (2020) studied a heavy precipitation process in the Yangtze River Basin and suggested that after the cloud cluster had formed and moved out of the Qinghai–Tibetan Plateau, liquid-phase processes, riming, and aggregation processes all significantly increased, which increased the particle size combined with the moisture transport in the low levels to produce heavy precipitation. In general, water vapor in the upper troposphere plays a role that is not less important than that at low levels in forming heavy precipitation, especially when associated with tropical cyclones.

Numerical weather forecasting has played an increasingly important role in precipitation forecasting in recent years (Liguori et al., 2012). The Weather Research and Forecasting (WRF) model is widely used in both atmospheric research and operational forecasting (Evans et al., 2012; Tian et al., 2017; Yin et al., 2022). The WRF model simulates temperature, air pressure, humidity, wind, and other variables well (Sharma et al., 2017). Humidity is an important parameter characterizing the amount of atmospheric water vapor. Many sensitivity experiments have indicated that the path and intensity of tropical cyclones are greatly affected by changes in environmental humidity (Wu et al., 2012; Yan et al., 2017). Microphysical processes are described by different parameterization schemes in the WRF model. Tian et al. (2021) showed that the results simulated by the model may be significantly different if different parametrization schemes were selected. The microphysical schemes selected to yield the most accurate forecast compared with real-time observations are not necessarily the same for different heavy precipitation events (Huang et al., 2020). With the WRF model, we can conduct sensitivity experiments by modifying the moisture profile to clarify the role of moisture in the upper levels.

Despite the extensive research on moisture transport, there remains a limited emphasis and comprehension regarding the impact of mid-to-upper-level transport and the underlying mechanisms of heavy precipitation events. To address these issues, we conducted sensitivity experiments on the transport height of water vapor using the WRF model. Specifically, we conducted a case study focusing on Super Typhoon Mangkhut (2018) and analyzed the associated mechanisms.

2. Case overview and methods

Super Typhoon Mangkhut (2018) made landfall along the coast of Taishan City, Guangdong Province, China, at approximately 09:00Z on September 16, 2018. The maximum average wind speed near the center of the tropical cyclone was 45 m/s. It gradually weakened after landfall. The super typhoon not only brought rainstorms to the coast of southern China but also caused heavy rainfall in the Yangtze River Delta, resulting in huge losses to property. The contours in Fig. 1 show the vertical integrals of the water vapor flux during the simulation period retrieved from ERA5 data (Hersbach et al., 2020). Apart from the large moisture transport in the main body of the typhoon (southwest of d03; over 500 kg m^{-1} s^{-1}), large values of water vapor flux were observed in the southeast of d03, mostly exceeding 300 kg m^{-1} s^{-1}. The moisture transport belt separated from the main body of the typhoon transported warm moist air northward to the study area, providing favorable conditions for the generation of heavy rainfall.

Yu et al. (2020) suggested a clear boundary between the main body of the typhoon and the remote precipitation area, where the reflectivity exceeded 35 dBZ and precipitation persisted for more than 6 h. The moisture transported to the Yangtze River Delta gradually separated from the main body of the typhoon, which played a crucial role in transporting moisture mainly from the Philippine Sea, the sea south of the Philippines, and the southern South China Sea, to the heavy precipitation area according to their backward trajectories for air parcels. Numerical experiments conducted by Jiang et al. (2022) showed that the larger the scale of Typhoon Mangkhut, the larger the high-humidity area and higher the convergence layer, indicating that the typhoon was closely associated with moisture in the heavy precipitation area.

The domains of the WRF (version 4.0) model where we conducted sensitivity experiments, and the track of Typhoon Mangkhut are shown in Fig. 1. The initial and boundary conditions for the numerical simulation were obtained from the Global Forecasting System analysis dataset of the National Centers for Environmental Prediction (NCEP GFS-ANL) with a resolution of (0.5° × 0.5°), 32 isobaric surfaces in the vertical direction, and 4 soil layers. The path data of Typhoon Mangkhut were obtained from the China Meteorological Administration Tropical Cyclone Data Center's Best Track Dataset (tcdata.typhoon.org.cn) (Lu et al., 2021; Ying et al., 2014). Fig. 1 shows the path of the typhoon as a blue line. The initial data was provided at 6-h intervals. The integration time step was set to 45 s, and the output time interval was 1 h. The simulation period was from 00:00Z on September 16, 2018, to 00:00Z on September 18, 2018. The simulation area included a parental domain

Table 1
Relationship of water vapor in each layer between after adjustment and before adjustment in each trial.

Trial	Relationship
1	$m_1(i) = m_0(i)$
2	$m_1(i) = 0.7m_0(i) + 0.3m \cdot weight(i)$
3	$m_1(i) = [m - m_1(j) - m_1(k)]\frac{m_0(i)}{m - m_0(j) - m_0(k)} (i \neq j, i \neq k)$

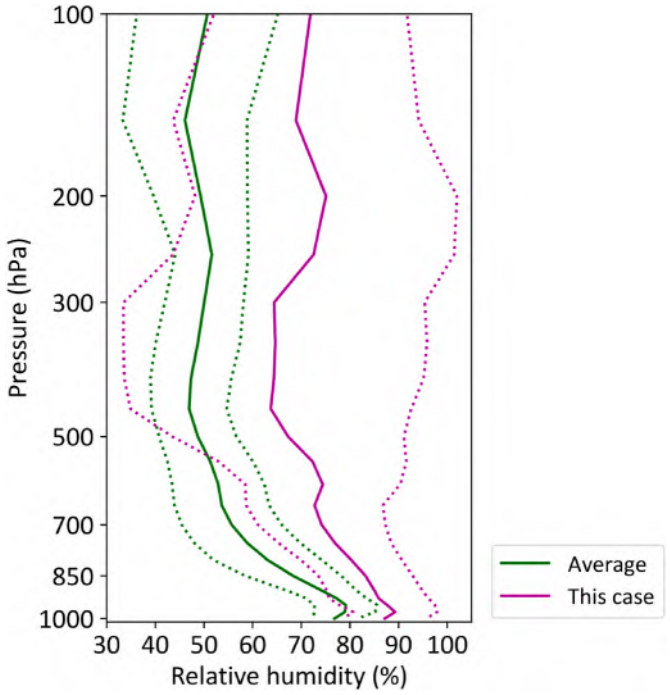

Fig. 2. Variation in the average relative humidity with height in d03 (units: %). The solid and dotted green lines are the average and average plus (minus) standard deviation calculated from September 1981 to September 2010, respectively. The solid and dotted purple lines are the average and average plus (minus) standard deviation from September 16, 2018 to September 17, 2018, respectively. (For interpretation of the references to colour in this figure legend, the reader is referred to the Web version of this article.)

and two nested domains, which were two-way nested (d01, d02, and d03, respectively, as shown in Fig. 1). The Yangtze River Delta (where heavy precipitation occurred) was included in d03, and the path of the typhoon during the simulation period was included in d02 to capture the distribution and associated processes in the heavy precipitation area, as well as the large-scale circulation background. The horizontal resolution of the parent domain was 9 km, whereas the nested domains had horizontal resolutions of 3 km and 1 km. The sizes of d01, d02, and d03 were approximately 3411 km (west-east, the same below) × 2691 km (south-north, the same below), 2178 km × 1926 km, and 843 km × 963 km, respectively. We used the Lambert projection in this simulation.

We selected the WSM6, KF, and RRTMG parameterization schemes as the microphysical, cumulus, and longwave/shortwave radiation schemes, respectively. These schemes perform best when used together in precipitation forecasts associated with tropical cyclones on the southeast coast of China (Tian et al., 2021). We selected Yonsei University (Hong et al., 2006) and the unified Noah land surface model (Tewari et al., 2004) as the planetary boundary layer and land surface schemes, respectively, since both schemes perform well in the WRF model and have been widely applied for rainfall simulations (Ahasan and Khan, 2013; Srivastava et al., 2015; Yin et al., 2022).

We conducted the following trials: (the "layer" in the descriptions represents the three-dimensional area between two adjacent isobaric levels. There were 31 layers because there were 32 isobaric levels in the vertical direction.)

1. We used the settings above to simulate the CTRL run.
2. Ensuring that the total mass of water vapor in the vertical column (from the ground to 10 hPa) corresponding to each grid point was constant, we changed the moisture profile in d03 by altering the relative humidity of each layer such that the vapor mass in each layer maintained the same proportion to the total water vapor mass of the column as the average proportion observed in d03 during September 1981–2010.
3. Ensuring that the total mass of water vapor in the vertical column corresponding to each grid point was constant, we changed the moisture profile in d03 such that the water vapor in the adjacent two layers was saturated after each adjustment. The remaining water vapor in the column was weighed and distributed to the other layers according to the proportion of the water vapor mass in each layer. The layers where water vapor was saturated after each adjustment were: 1000–950; 950–900; 900–800; 800–700; 700–600; 600–500; 500–400; and 400–300 hPa.

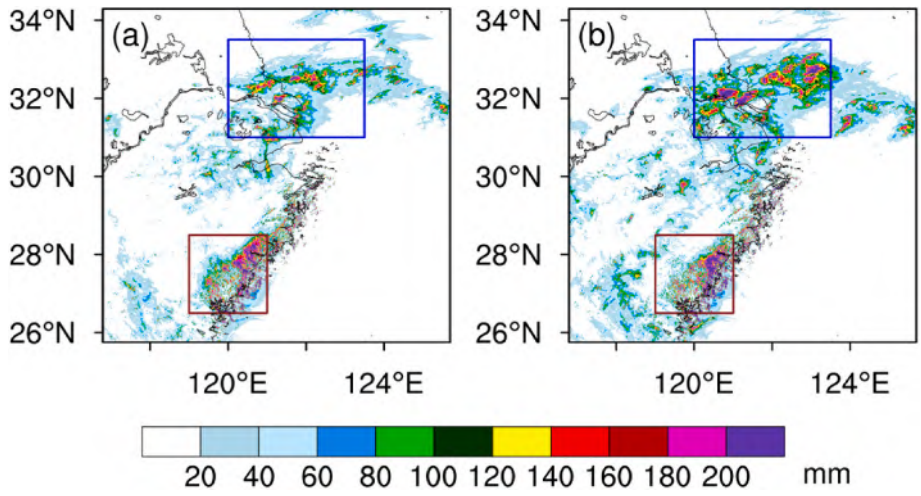

Fig. 3. Distribution of total precipitation (units: mm) simulated in (a) Trial 2 and (b) Trial 1 (CTRL) from 00:00Z on September 16, 2018 to 00:00Z on September 18, 2018.

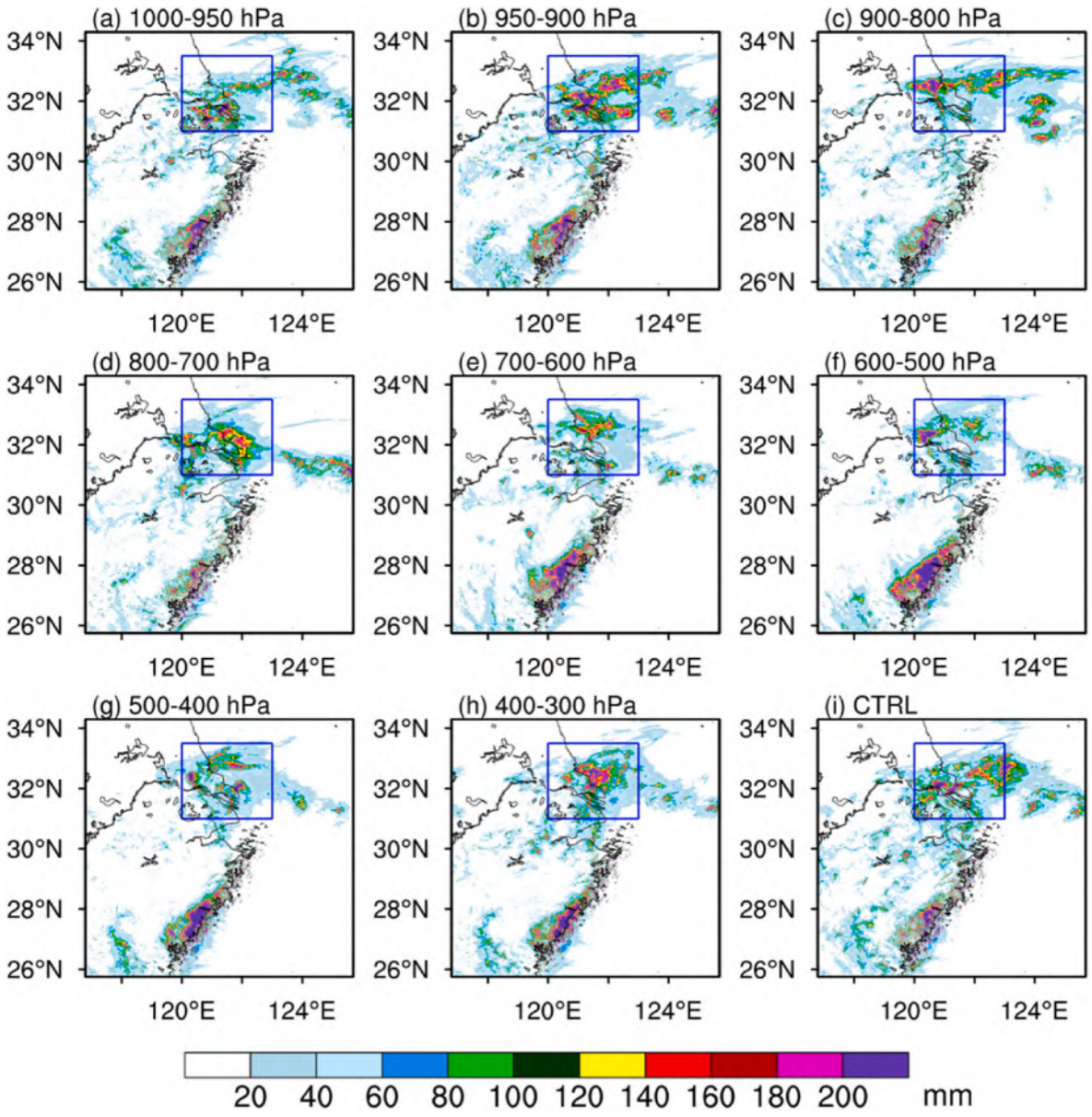

Fig. 4. Distribution of total precipitation (units: mm) simulated in Trials 3 and 1. The layers where water vapor is adjusted to saturation are (a) 1000–950, (b) 950–900, (c) 900–800, (d) 800–700, (e) 700–600, (f) 600–500, (g) 500–400, and (h) 400–300 hPa, and (i) CTRL.

Table 1 shows the relationship between the water vapor in each layer before and after adjustment in each trial, where $m_0(i)$ is the original mass of water vapor in layer i, $m_1(i)$ is the mass of water vapor in layer i after adjustment, m is the total mass of water vapor in the column, and weight (i) is the proportion of the average mass of water vapor in layer i in d03 to that in the column during September 1981–2010. It is assumed that layers j and k are saturated after adjustment in Trial 3.

3. Results

3.1. Comparison of the water vapor profiles in d03

Fig. 2 shows the average moisture profiles in September from 1981 to 2010 and September 16 to September 17, 2018, in d03 using the ERA5 reanalysis data (Hersbach et al., 2020). The values obtained after adding and subtracting the standard deviation from the average values are also shown. The annual mean relative humidity was the highest at approximately 950 hPa and then decreased as the height increased. At 500–100 hPa, the relative humidity fluctuated around 50%, with the standard deviation of the entire column stable at approximately 10%. During this precipitation process, the average relative humidity of each layer was significantly higher than the annual mean by 10–30 percentage points, and the difference was greater in the mid-to-upper levels. The difference between the average value of the process and the annual mean showed a bimodal feature, with one peak near 600 hPa and the other near 200 hPa. The standard deviations of the relative humidity were greatest in mid-levels, with the span between the maximum and minimum values being >60%, which indicated that the data were diverged. Therefore, the overall water vapor content in this area during the precipitation process was significantly higher than the annual mean, and the discrepancy in the moisture transport in the mid-to-upper levels should not be neglected.

3.2. Comparison between the simulation results in Trials 1 and 2

Fig. 3 shows the results of the simulated 48-h total precipitation distribution of Trial 2 after adjusting the water vapor content of each layer according to the average moisture profile in d03 in September

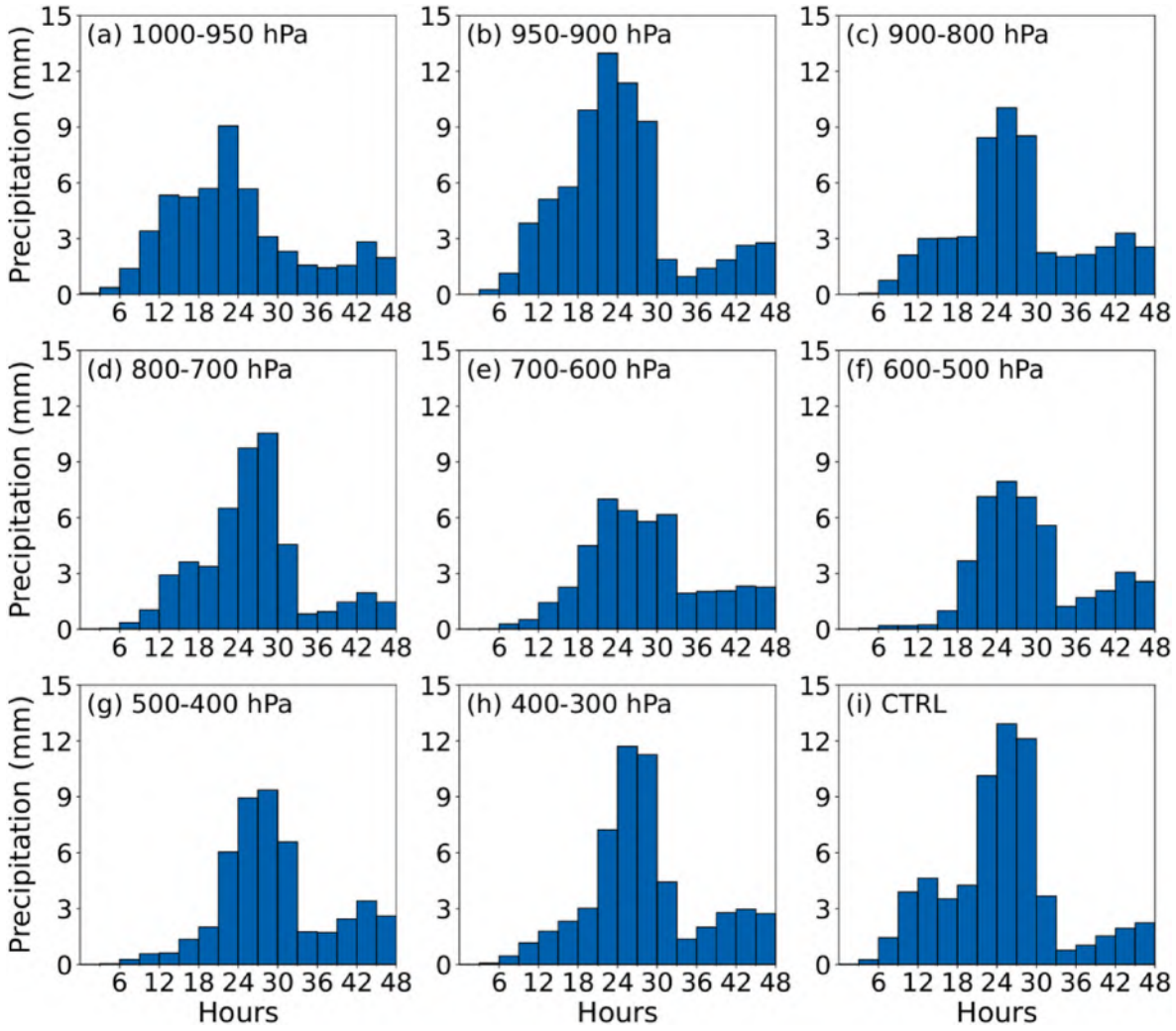

Fig. 5. Three-hour variation of average single-grid precipitation (units: mm per grid point) calculated from all grid points within blue rectangles in Fig. 4 simulated in Trials 3 and 1. The layers where water vapor is adjusted to saturation are (a) 1000–950, (b) 950–900, (c) 900–800, (d) 800–700, (e) 700–600, (f) 600–500, (g) 500–400, (h) 400–300 hPa, and (i) CTRL. The horizontal axis represents the time elapsed from 00:00Z on September 16, 2018, and the vertical axis represents the average 3-h precipitation of the selected grid points. (For interpretation of the references to colour in this figure legend, the reader is referred to the Web version of this article.)

from 1981 to 2010 (Fig. 3a) and in Trial 1 (CTRL; Fig. 3b). In Trial 1, heavy precipitation occurred primarily in two areas. One was the northern precipitation area, located near the coastline of the Yangtze River Delta and the sea surface to its east (blue rectangles in Fig. 3). The area of heavy precipitation (>140 mm) was discrete, with precipitation >200 mm in areas near (32° N, 120.5° E) and (33° N, 122.5° E). The southern precipitation area was located at 26.5–28.5° N, 119–121° E (brown rectangles in Fig. 3), where the total precipitation was generally >140 mm and locally >200 mm. Rainfall also occurred in other areas but had a lower intensity. The heavy precipitation in these two areas corresponds well with the large values of moisture transport reported in other studies (Yu et al., 2020). We compared it with the precipitation amount retrieved by the Integrated Multi-satellite Retrievals for the GPM (IMERG) Final Run precipitation dataset, which merges satellite microwave precipitation estimates together with microwave-calibrated infrared satellite estimates and precipitation gauge analyses and has good quality over mainland China (Hou et al., 2014; Tang et al., 2016). The correlation coefficient when they are both averaged at 1-degree intervals in d03 is 0.61, indicating that CTRL is capable of reproducing the approximate distribution and intensity of this precipitation event.

After adjusting the water vapor content, the coverage of the southern precipitation area changed slightly, although the intensity was slightly lower. As for the northern precipitation area, the area with rainfall >150 mm is significantly smaller, that is, the 2020 and 6059 model grid points in blue rectangles in Fig. 3a and b, respectively. The maximum precipitation amounts were 460 mm and 656 mm, respectively, demonstrating that the precipitation intensity was higher in Fig. 3b (CTRL). The areal coverage of heavy precipitation over the sea in the northern area was much smaller than that in Trial 1. The areal coverage of heavy rainfall on land was reduced, with a total rainfall amount of only >200 mm near (32° N, 121° E). In general, after adjusting the transport height of water vapor, the overall precipitation and areal coverage of heavy precipitation were both significantly reduced, indicating that different transport heights of water vapor led to significant differences in the spatial distribution and total precipitation in the study area.

3.3. *Comparison between the simulation results in Trials 1 and 3*

The 48-h total precipitation results were significantly different when the water vapor in different layers was adjusted to saturation (Trial 3; Fig. 4). The location of heavy precipitation was consistent with the northern and southern precipitation areas shown in Fig. 3. Heavy

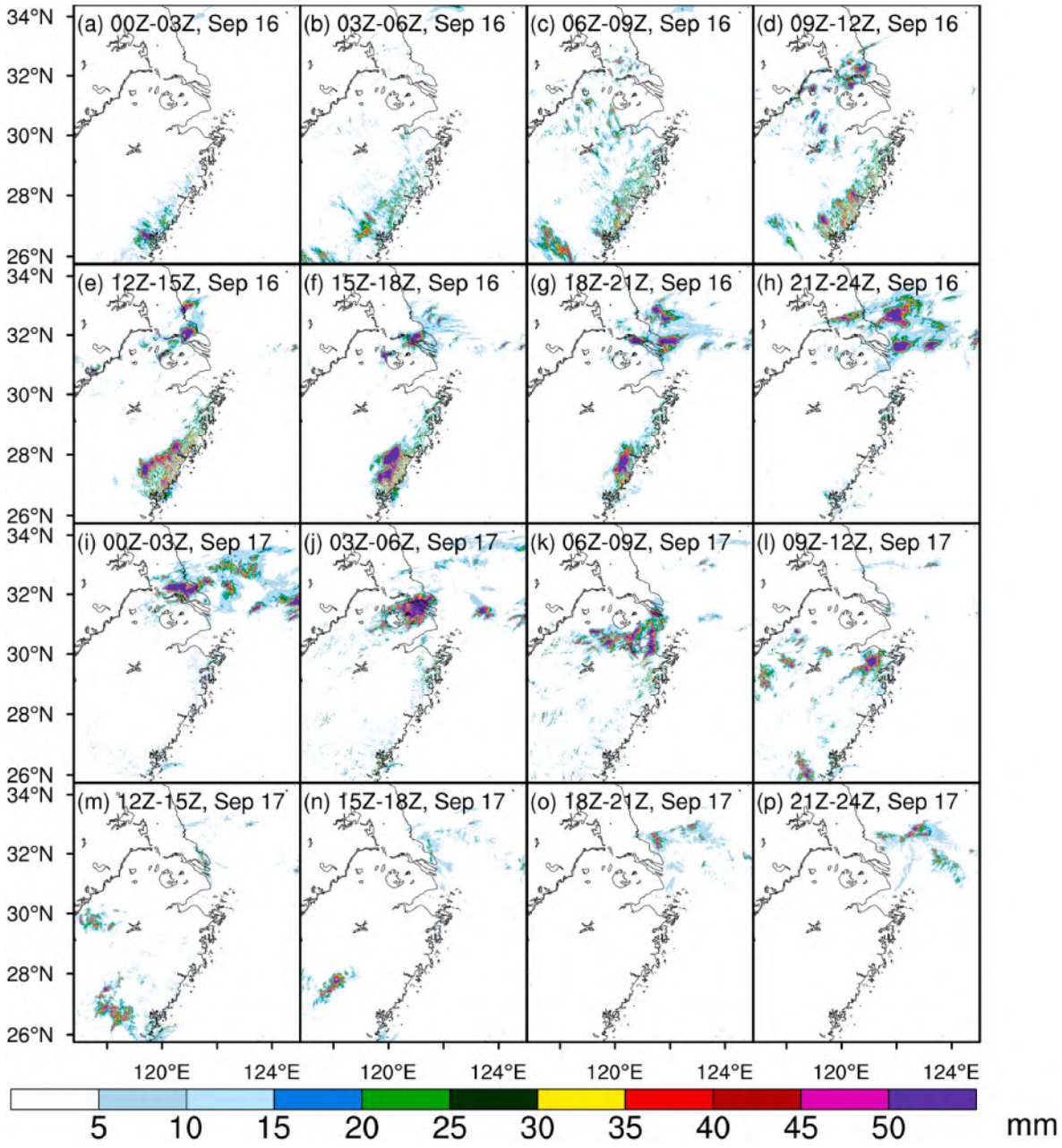

Fig. 6. Three-hourly variation of the simulated total precipitation after adjusting the water vapor at 950–900 hPa to saturation.

precipitation in the northern precipitation area was mainly observed in areas marked with blue rectangles in Fig. 4. When the water vapor was saturated at 950–900 hPa, the precipitation was largest in the northern precipitation area, and the largest cumulative rainfall was >200 mm (Fig. 4b). In contrast, when the water vapor was saturated at 700–600 hPa, the precipitation was lowest in the northern area, generally <100 mm, and only >140 mm near (32.5° N, 121° E) (Fig. 4e). The simulation results also show that when 950–900 hPa was saturated, the overall precipitation in the northern precipitation area significantly exceeded that in Trial 1, whereas it was significantly weaker than in Trial 1, when the saturation height of the water vapor was between 700 and 400 hPa and was generally <100 mm (Fig. 4e–h). For the southern precipitation area, the overall precipitation was significantly stronger than in Trial 1, when the transport height was between 700 and 300 hPa. The simulation results of precipitation were similar to those of Trial 1, when the saturation height was below 700 hPa.

We plotted a 3-h variation diagram of the average precipitation at a single grid point to further explore the differences in precipitation in different periods caused by different transport heights of water vapor (Fig. 5). We selected grid points in the northern precipitation area, including both the land and sea areas (blue rectangles in Fig. 4). The precipitation trend for each period can be observed. The peak time of the average precipitation in the region was from early morning to noon (local time), which was probably a result of the boosting effect of the sea-land breeze (Huang et al., 2010; Yuan et al., 2012). When 1000–950 hPa was saturated, the period with the strongest precipitation was relatively early, from hours 21–24 (21:00Z–24:00Z) (Fig. 5a). With a gradual increase in the transport height of water vapor, the strongest precipitation period was gradually delayed.

When 800–700 hPa was saturated, the strongest precipitation period was from hours 27–30 (03:00–06:00Z) (Fig. 5d). If the height continued to increase to 700–600 hPa, the strongest precipitating period advanced to hours 21–24, while the period of strongest precipitation became later with increasing transport heights (Fig. 5f–h). These results indicate that

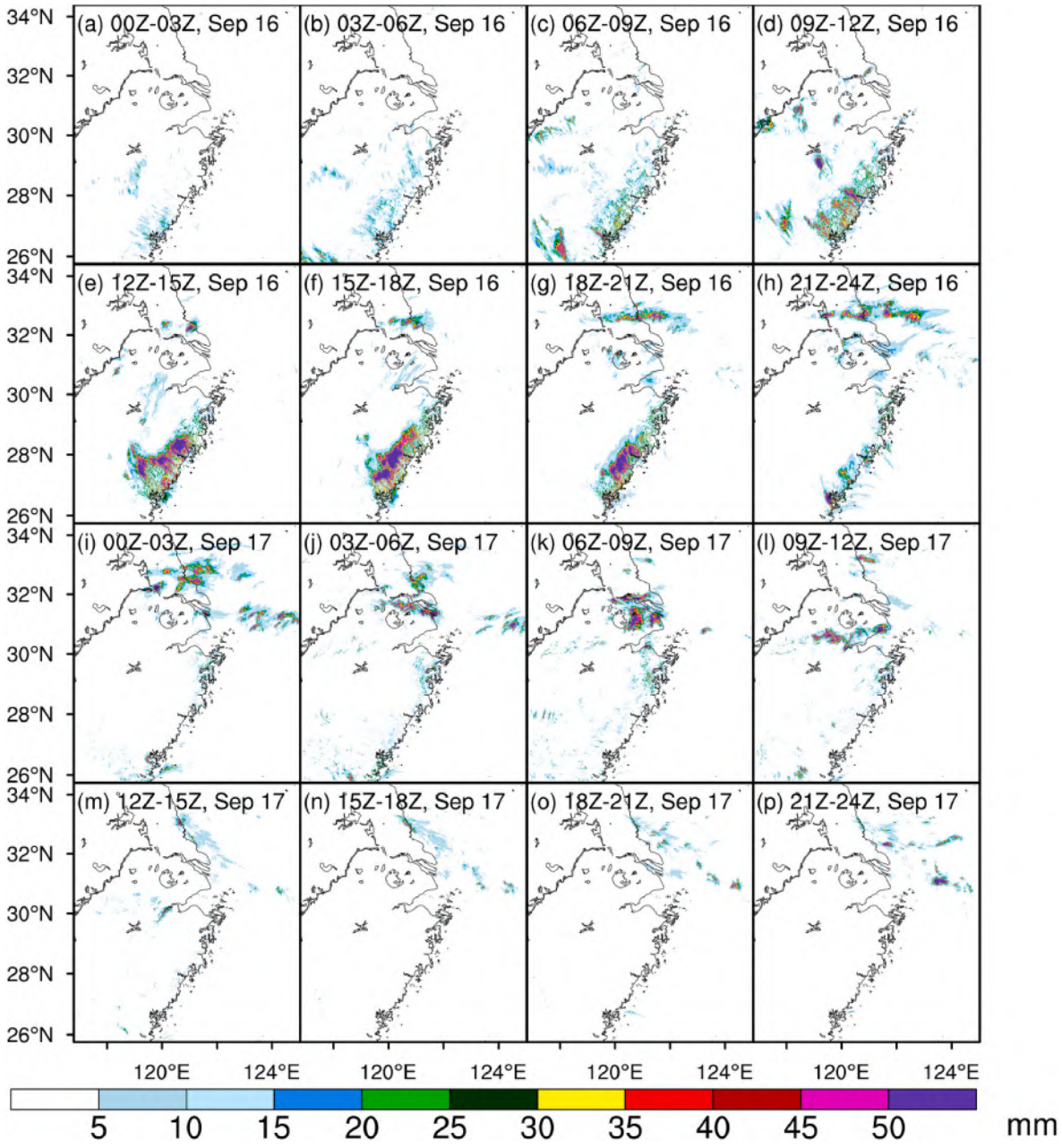

Fig. 7. Three-hourly variation of the simulated total precipitation after adjusting the water vapor at 700–600 hPa to saturation.

the period of the strongest precipitation changed periodically with the increase in the transport height of water vapor.

In terms of precipitation intensity, except for Trial 1 (CTRL), the average 3-h precipitation per grid point was largest when 950–900 hPa was saturated (Fig. 5b) and was approximately 13 mm per grid point. Precipitation had a long duration, and the average value was >9 mm for 12 consecutive hours. In comparison, when 700–600 hPa was saturated, there was no period when the average precipitation in 3 h was >9 mm (Fig. 5e), indicating that the overall precipitation was weaker. When 400–300 hPa was saturated, the 3-h average precipitation during hours 24–30 was >10 mm, and the temporal distribution of precipitation was closer to that in the CTRL run (Fig. 5h and i).

We selected three numerical experiments, in which the transport heights of water vapor were different, to explore the differences in the spatial distribution of precipitation every 3 h. The three experiments adjusted the water vapor at 950–900 hPa, 700–600 hPa, and 400–300 hPa to saturation. Figs. 6–8 show the spatial distribution of precipitation in d03 every 3 h.

When 950–900 hPa was saturated (Fig. 6), the northern precipitation area experienced heavy precipitation primarily between 09:00Z on September 16, 2018, and 12:00Z on September 17, 2018. This area consisted of two precipitation centers, one on land (32° N, 121° E) and one over the sea (32° N, 122° E). There were 5331 model grid points with precipitation >50 mm in 3 h when the precipitation was heaviest in the northern precipitation area (Fig. 6d–l). The center of precipitation on land moved from (32° N, 120.5° E) to (29.5° N, 121° E) and then weakened and disappeared. The center of precipitation at sea moved from (32.5° N, 121° E) to (31.5° N, 123° E), the range of which decreased with time. It rained earlier in the southern precipitation area, mainly from 17:00Z on September 16, 2018, to 05:00Z on September 17, 2018, and the precipitation was generally moderate, with approximately 20 mm every 3 h (Fig. 6d– g). After this period, precipitation gradually weakened and disappeared.

When 700–600 hPa was saturated (Fig. 7), precipitation mainly

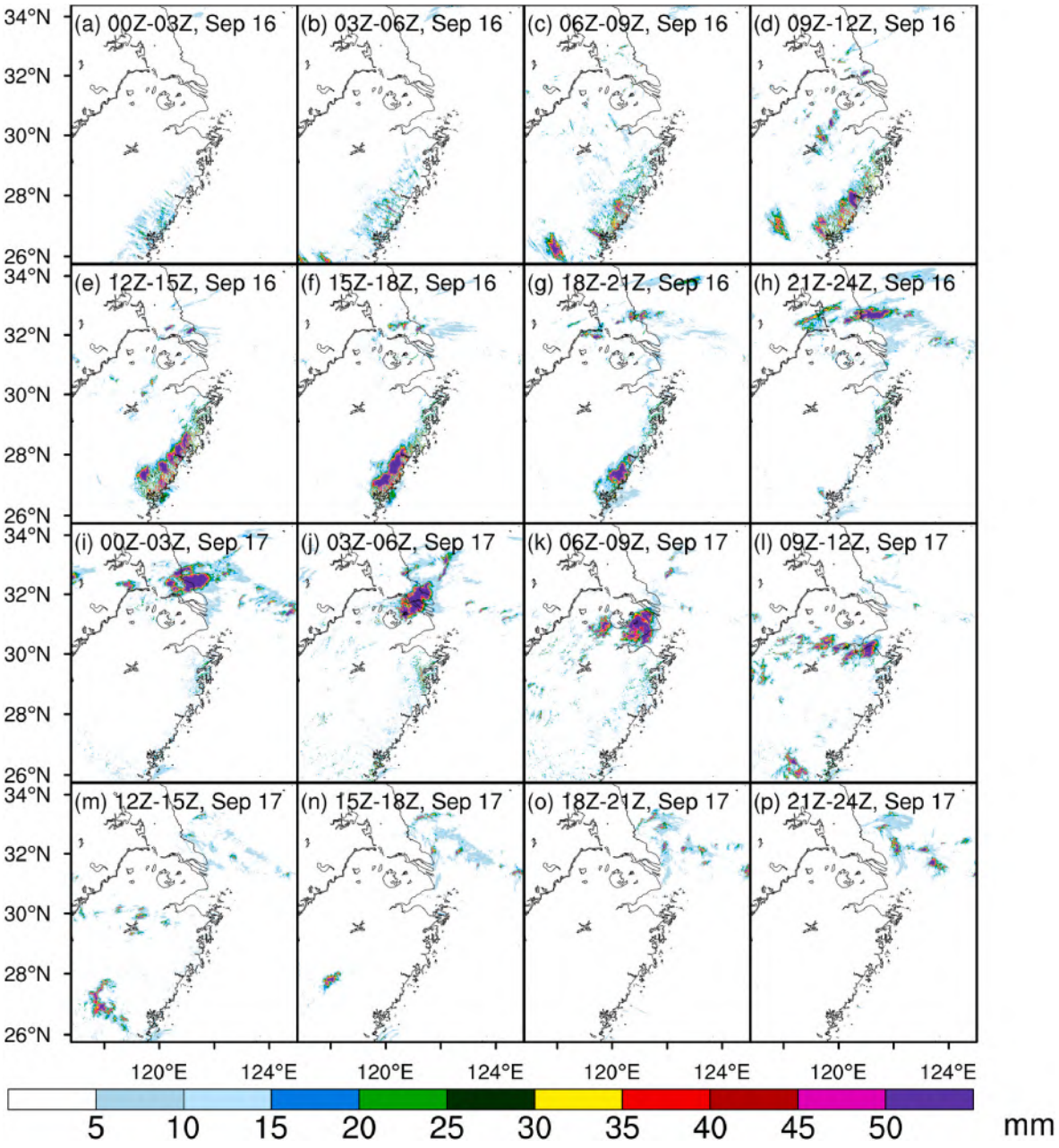

Fig. 8. Three-hourly variation of the simulated total precipitation after adjusting the water vapor at 400–300 hPa to saturation.

occurred between 12:00Z on September 16, 2018, and 12:00Z on September 17, 2018, as in the northern precipitation area. The area could still be divided into two parts, one located near (32.5° N, 120.5° E), with precipitation occurring earlier than in the other part and reaching 40 mm in 3 h. The other part was located near (31.5° N, 121° E), with precipitation occurring mainly during the day on September 18, 2018. The intensity of precipitation was strong, but of short duration, with 2923 model grid points having >50 mm precipitation in 3 h when the precipitation was the heaviest (Fig. 7e–l). Heavy precipitation in the southern precipitation area generally occurred from 12:00Z to 21:00Z on September 16, 2018. The number of model grid points near (28° N, 120° E), where the 3-h total precipitation was >50 mm, reached 4204 (Fig. 7e– g).

When 400–300 hPa was saturated (Fig. 8), the heavy precipitation period was mainly between 21:00Z on September 16, 2018, and 12:00Z on September 17, 2018. Precipitation increased significantly during the day, with 5633 model grid points having >50 mm precipitation in 3 h, but the duration was not long. Precipitation rapidly weakened at night. Precipitation in the southern precipitation area mainly occurred during the night of September 16, 2018, and weakened significantly during the day.

In terms of precipitation in the CTRL run (Fig. 9), we calculated the distribution of the 3-h precipitation in Trial 1. The period of precipitation in the southern precipitation area during the CTRL run was slightly different from that in the other trials, but the overall precipitation was much lighter than in the other experiments (Fig. 9e– g). Precipitation in the northern precipitation area was mainly observed from 21:00Z on September 16, 2018, to 12:00Z on September 17, 2018 (Fig. 9h–l), with precipitation in 7080 model grid points >50 mm in 3 h when precipitation was the heaviest. The center of precipitation moved from (32° N, 120° E) to (29.5° N, 120.5° E) and the intensity weakened rapidly.

We have compared Figs. 6–9, focusing mainly on heavy precipitation in the northern precipitation area. Heavy precipitation occurred earliest when 950–900 hPa was saturated and latest when 400–300 hPa was

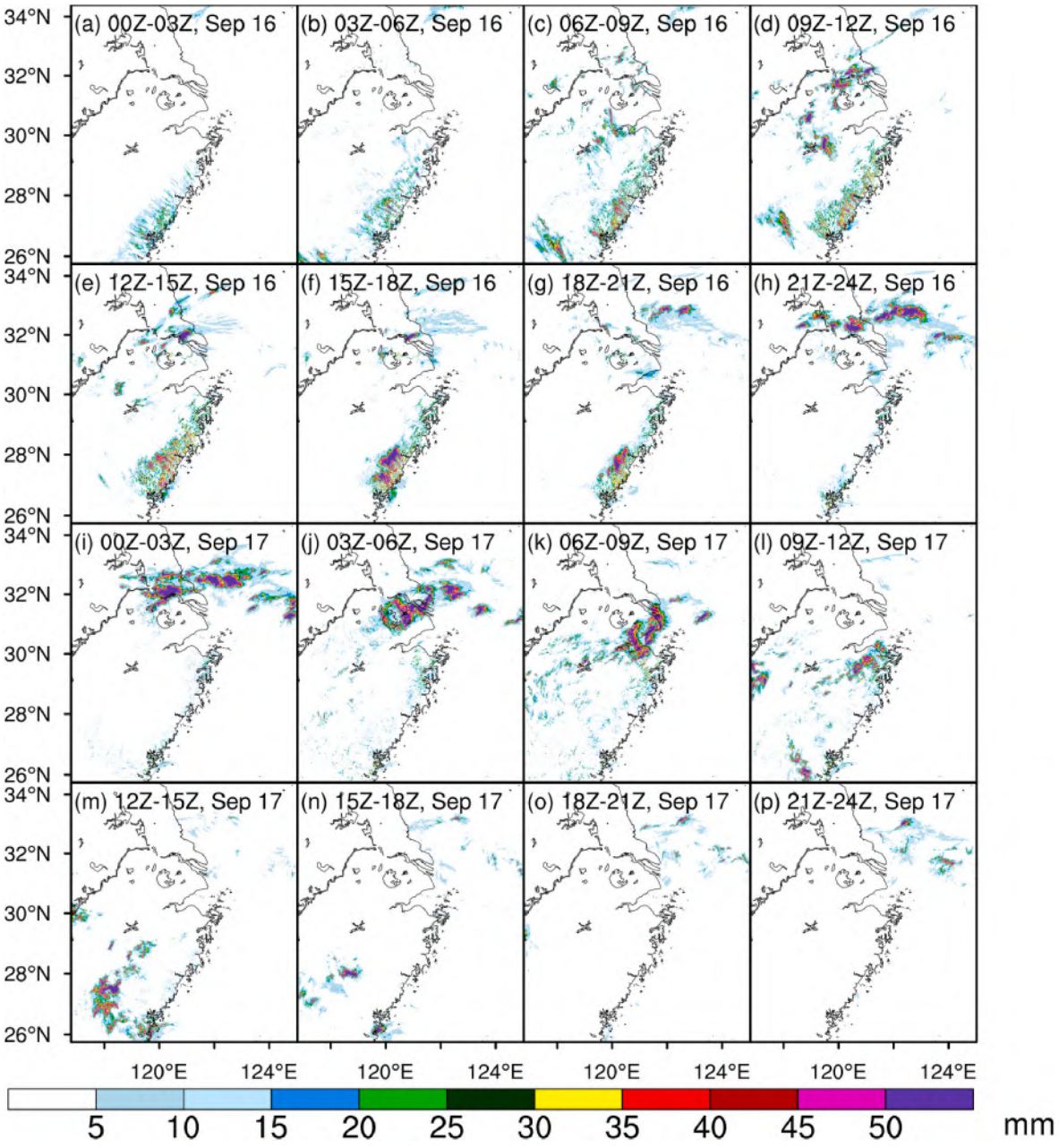

Fig. 9. Three-hourly variation of the simulated total precipitation for Trial 1 (CTRL run).

saturated. The amount of precipitation in the CTRL run was between that when 950–900 hPa was saturated and when 400–300 hPa was saturated. The amount of rainfall was the lowest when 700–600 hPa was saturated. The precipitation in all experiments generally moved from north to south. We conclude that different transport heights of water vapor led to significant variations in the distribution, intensity, and duration of heavy precipitation.

3.4. Mechanisms

The mechanisms leading to the differences in the distribution of heavy precipitation are discussed below. Figs. 10 and 11 show the variation with time in the mixing ratio of (cloud water + cloud ice) and (rain + snow + graupel), respectively, averaged in the blue rectangles in Fig. 4. Hour 0 represents 00:00Z on September 16, 2018. The mixing ratio of each variable represents the relative content in the atmosphere. The maximum values of the cloud-water mixing ratio in the 4 trials were almost the same (>0.08 g/kg), and the periods in which they reached their peak values were also similar. When 950–900 hPa or 700–600 hPa was saturated, heavy precipitation mainly occurred in hours 18–30. In contrast, in the CTRL run and when 400–300 hPa was saturated, heavy precipitation mainly occurred during hours 21–30.

When 950–900 hPa was saturated (Fig. 10a and 11a), the cloud ice mixing ratio was high during hours 15–18, but there was little precipitation at this time. When the cloud water mixing ratio at mid-to-low levels was high, the rainwater mixing ratio also reached a large value (>0.15 g/kg). The amount of cloud ice reached a peak in hours 27–30, and the mixing ratio of the frozen hydrometeors at mid-to-upper levels reached a peak (>0.4 g/kg), but the rainwater mixing ratio decreased with decreasing height during this period, indicating that the evaporation process occurred at lower levels. The peak value of the rainwater mixing ratio corresponded to the peak value of cloud water rather than cloud ice, indicating that the ice-phase processes contributed less to the heavy precipitation in Trial 3 than the liquid-phase processes when the

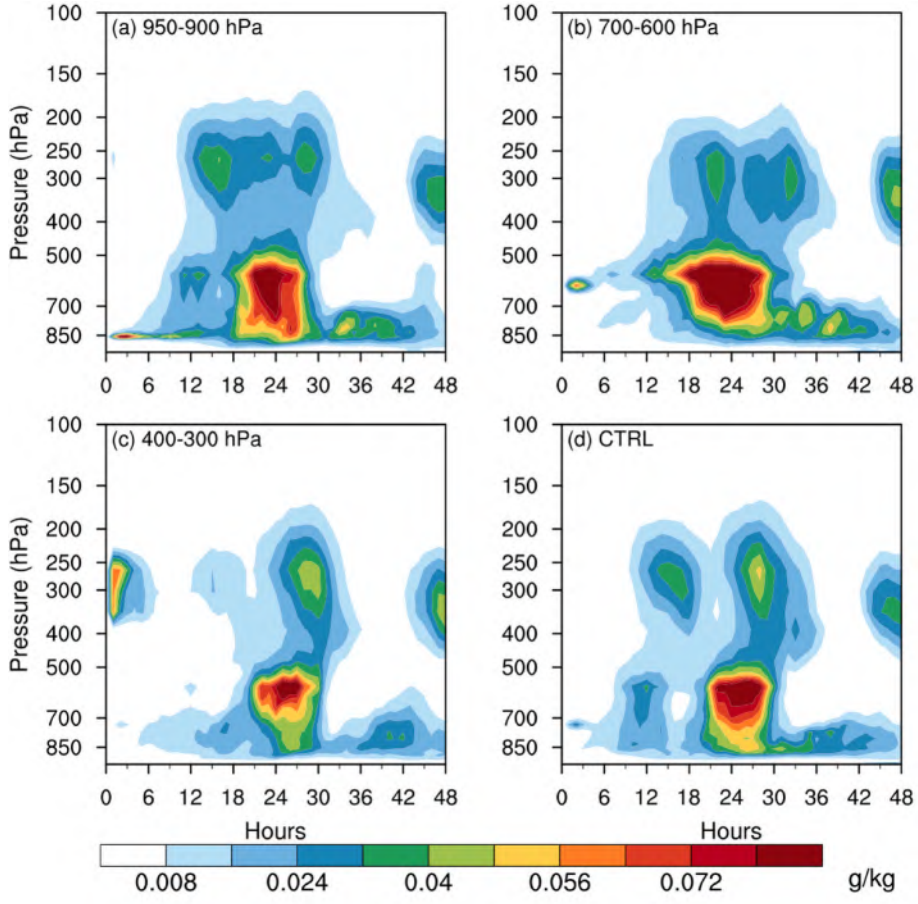

Fig. 10. Variations of the sum of cloud water and cloud ice mixing ratios (units: g/kg) averaged in the blue rectangles in Fig. 4 with time (units: hours). The layers where the water vapor is adjusted to saturation are: (a) 950–900 hPa; (b) 700–600 hPa; and (c) 400–300 hPa; (d) CTRL run. (For interpretation of the references to colour in this figure legend, the reader is referred to the Web version of this article.)

water vapor was saturated at 950–900 hPa. The droplets in clouds grew into raindrops through microphysical processes such as condensation and coalescence before falling to the ground. The increase in the rain rate was affected by the increase in the particle size and high mixing ratio of rainwater (Niu et al., 2010). This analysis implies that heavy precipitation was dominated by liquid-phase processes.

The results varied significantly when 700–600 hPa was saturated (Fig. 10b and 11b). There were two peaks in the cloud ice mixing ratio in the mid-to upper levels: one in hours 21–24 and the other in hours 30–33. The cloud water mixing ratio at 850 hPa, corresponding to the first peak, was relatively low, weakening liquid-phase processes. Precipitation was probably induced by ice particles, which were generated in the mid-to-upper levels and grew through ice-phase processes before melting into rainwater near the 0 °C layer. At the second peak of the cloud ice mixing ratio, the mixing ratio of snow and graupel was much larger than that at the first peak and was >0.3 g/kg. However, at this time, the mixing ratio of (cloud water + cloud ice) at 500–700 hPa decreased significantly, although it increased below 700 hPa. The rainwater mixing ratio at the corresponding height decreased, indicating that most precipitation particles were generated at 250–400 hPa. After the ice particles fell to mid-to-low levels and melted, part of the rainwater evaporated, resulting in an increase in the cloud-water mixing ratio at approximately 700 hPa. Ice-phase processes were dominant microphysical processes in the second peak of heavy precipitation.

When 400–300 hPa was saturated (Fig. 10c and 11c), the cloud ice mixing ratio at mid-to-upper levels reached a peak value (0.4 g/kg) in hours 27–30. At this time, the mixing ratio of snow and graupel also reached a maximum (>0.45 g/kg), which suggested that many of the ice particles generated in the mid-to-upper levels grew through ice-phase processes before falling to lower levels and melting. The cloud water mixing ratio was at a peak (>0.08 g/kg) in hours 24–27. However, it was lower at 850 hPa and decreased rapidly after 27 h, indicating a weakening of the liquid-phase processes. Evaporation occurred at low levels, probably because of less effective conversion of cloud droplets to rainwater, which caused the vertical column to stabilize (Lin et al., 2011). The heavy precipitation in the areas where water vapor was saturated at 400–300 hPa was mainly caused by ice-phase processes.

Fig. 10d and 11d show the distribution of the mixing ratio of (cloud water + cloud ice) and precipitation in the CTRL run. The result was similar to that obtained when 400–300 hPa was saturated, but the values were larger. Therefore, the regional average precipitation was also larger (>12 mm/h) (Fig. 5i). The cloud ice in the mid-to-upper levels caused the peak value of frozen hydrometeors at 300–500 hPa (Fig. 11d), but the actual amount of precipitation did not increase. The heavy precipitation in the CTRL run was mainly caused by the joint influence of the liquid- and ice-phase processes. The above analysis confirms that a change in low-level humidity has a significant impact on the microphysical processes of precipitation (Zagrodnik et al., 2021).

The large mixing ratios of the hydrometeors were mainly observed from 18:00Z on September 16, 2018, to 06:00Z on September 17, 2018. Fig. 12 shows the vertical profiles of the liquid water content (LWC) and ice water content (IWC) at the 99th percentile, corresponding to the saturation of water vapor in different layers. The IWC obtained when 950–900 hPa was saturated was similar to that in the CTRL run and slightly higher than that when 400–300 hPa was saturated. This suggests that there were sufficient ice-phase processes in these three trials,

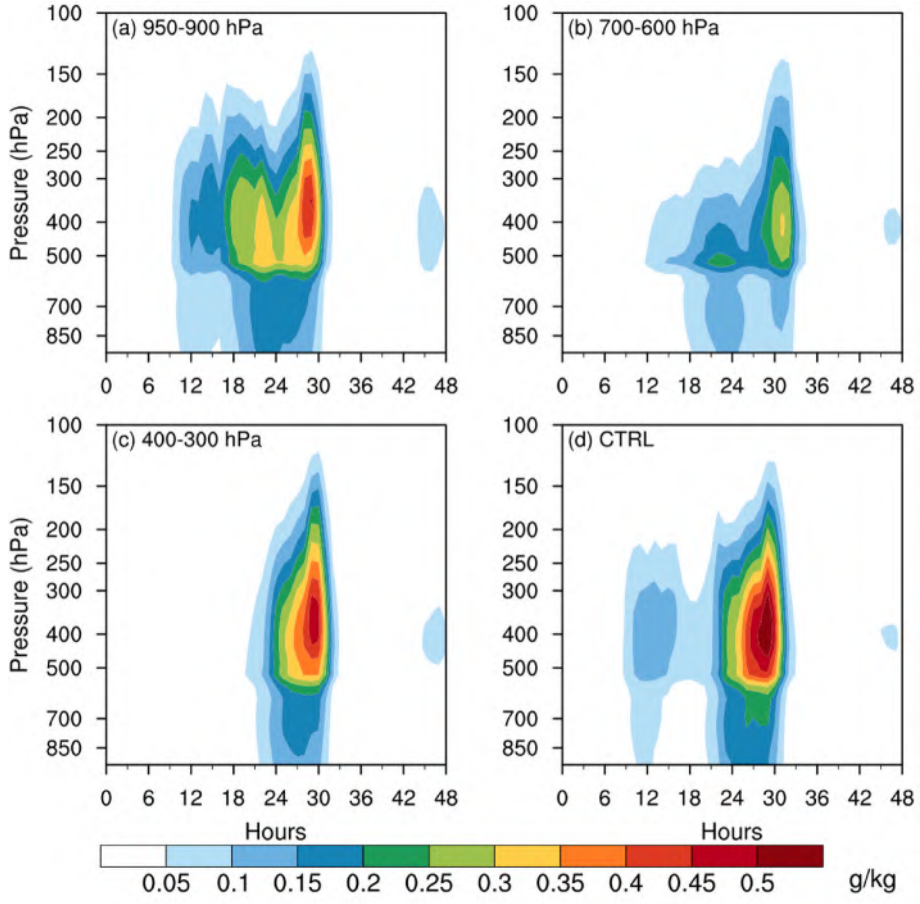

Fig. 11. Variations of the sum of rainwater, snow and graupel mixing ratios (units: g/kg) averaged in the blue rectangles in Fig. 4 with time (units: hours). The layers where the water vapor is adjusted to saturation are: (a) 950–900 hPa; (b) 700–600 hPa; and (c) 400–300 hPa; (d) CTRL run. (For interpretation of the references to colour in this figure legend, the reader is referred to the Web version of this article.)

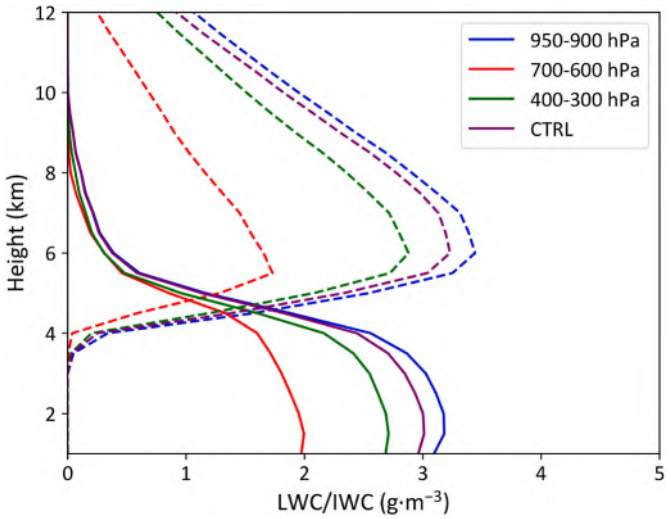

Fig. 12. Vertical profiles of the LWC (solid lines; units: g/m^3) and IWC (dashed lines; units: g/m^3) at the 99th percentile in blue rectangles in Fig. 4 from 18:00Z on September 16, 2018 to 06:00Z on September 17, 2018. Blue, red, green, and purple lines represent experiments where 950–900, 700–600 and 400–300 hPa were saturated and the CTRL run, respectively. (For interpretation of the references to colour in this figure legend, the reader is referred to the Web version of this article.)

probably resulting from the ice-phase processes caused by stronger updrafts, which enhanced precipitation (Han et al., 2021).

The vertical profiles of the LWCs for the four trials were similar to those of the IWCs, except that the large values were mainly observed at low levels. The differences in the maximum LWCs between the trials when 700–600 hPa was saturated and the other three trials were 0.7, 1 and 1.18 g/m^3, respectively, indicating that liquid-phase processes were most active when 950–900 hPa was saturated and most inactive when 700–600 hPa was saturated.

The IWCs were lowest when 700–600 hPa was saturated, indicating relatively weak convection and less precipitation. As shown in Supplementary Fig. 2, when 700–600 hPa was saturated, lower CAPE (less than 1500 J/kg) was seen in blue boxes, indicating a more stable atmospheric environment with less convective activity. This could be validated by θ_e (equivalent potential temperature) shown in Supplementary Fig. 4, where $\frac{\partial \theta_e}{\partial z} > 0$ between 700 hPa and 600 hPa during the first 18 h of the simulation. The result was also consistent with Takemi (2007), who suggested that when the column had a constant water vapor content, altering the moisture profile with a larger amount of water vapor at mid-levels and a smaller amount at low levels resulted in a more stable environment and weaker convective activity. The effectiveness of the conversion from ice particles to raindrops was low, probably because the moisture transport at 700–600 hPa neither promoted liquid-phase processes at low levels nor ice-phase processes in the upper levels. Consequently, ice particles in the upper levels could only aggregate and increase in size before melting in the 0 °C layer and falling to the ground. This was demonstrated in Supplementary Fig. 1 by less graupel and more snow and ice. When 400–300 hPa was saturated, the IWCs, particularly

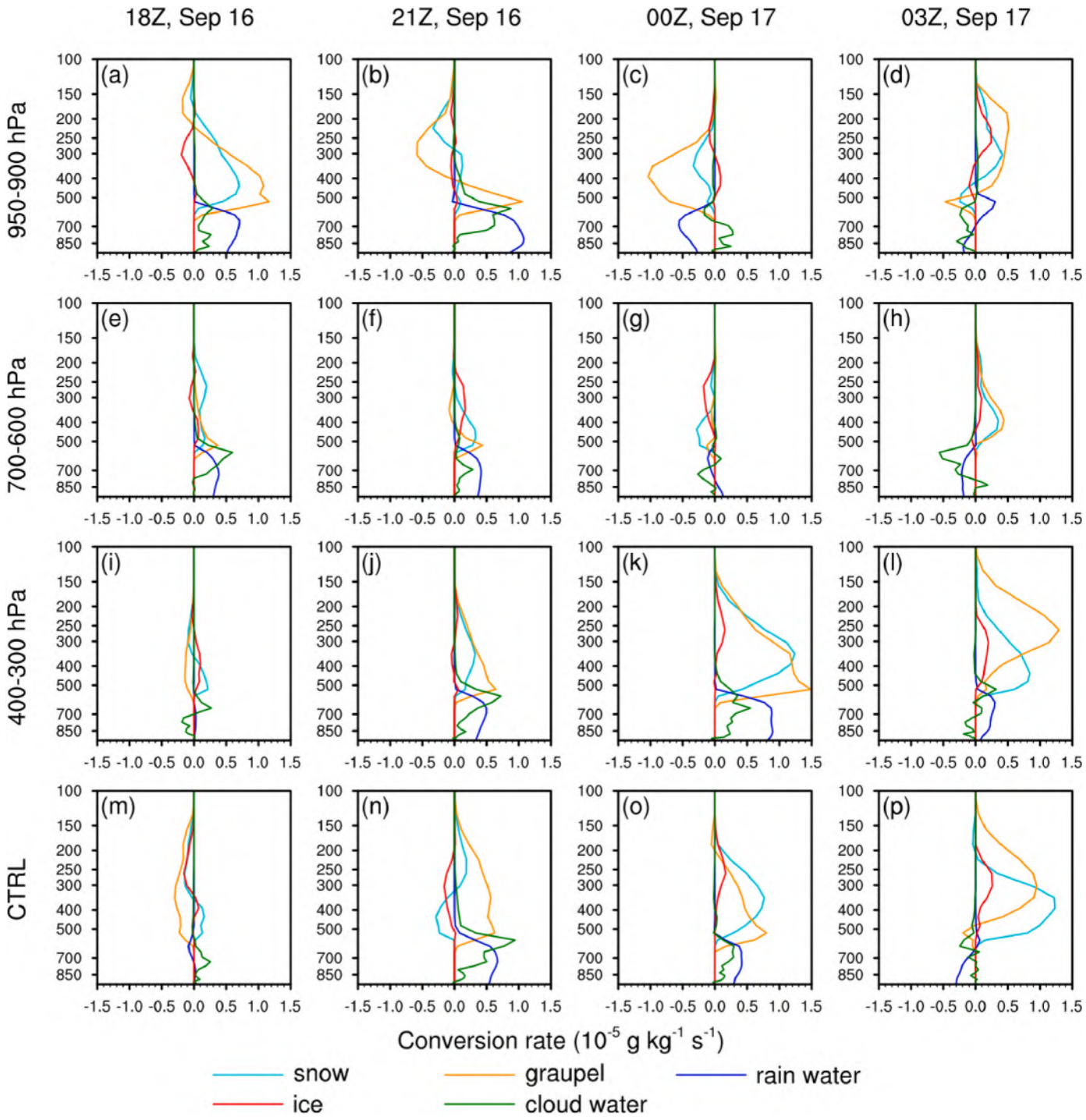

Fig. 13. Vertical profiles of hydrometeor conversion rates for trials: (a–d) 950–900 hPa; (e–h) 700–600 hPa; (i–l) 400–300 hPa; and (m–p) CTRL run.

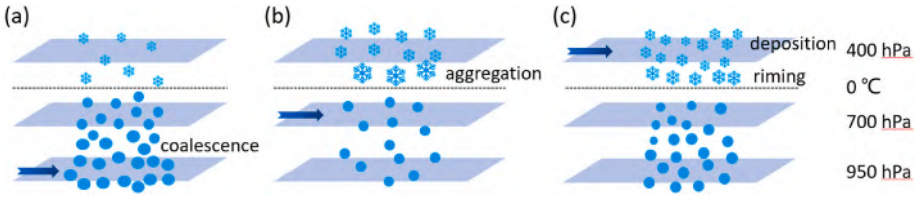

Fig. 14. Schematic diagram depicting the microphysical processes when water vapor was saturated at (a) 950–900 hPa, (b) 700–600 hPa, and (c) 400–300 hPa. The dark blue arrows represent the major moisture transport in the column. Blue circles/ellipses and snowflakes represent raindrops and ice particles, respectively. (For interpretation of the references to colour in this figure legend, the reader is referred to the Web version of this article.)

graupel, were larger than those in 700–600 hPa, indicating that deposition and riming processes were dominant. The LWC/IWC values in CTRL run fell between those observed in the 400-300 hPa trial and the 950-900 hPa trial, with close proximity between the values, which indicated again that both liquid-phase processes and ice-phase processes contributed to the precipitation observed in CTRL.

The vertical profiles of the hydrometeor conversion rates for each trial are shown in Fig. 13. The conversion rates of graupel at all four moments were comparatively low (under 0.5×10^5 g kg^{-1} s^{-1}) when 700–600 hPa was saturated (Fig. 13e–h), which validates the view that the aggregation process predominated during the ice-phase enhancement because ice crystals sticked together to form larger particles with little mass increase. Combined with Supplementary Fig. 2 and Supplementary Fig. 4, it is further indicated that less convection developed under the moisture profile in a more stable environment, such that precipitation was weaker compared with other trials. The conversion rates of snow and graupel at 400–300 hPa were the highest among those trials, with values close to 1.5×10^5 g kg^{-1} s^{-1} (Fig. 13k), indicating active ice-phase processes, especially deposition and riming. When 950–900 hPa was saturated, the higher conversion rate of cloud water (0.87×10^5 g kg^{-1} s^{-1}) in the mid-to-low levels, rather than the higher conversion rate of graupel, corresponded to a higher conversion rate of rainwater (1.08×10^5 g kg^{-1} s^{-1}) at low levels (Fig. 13a and b), confirming that the liquid-phase processes predominated.

The analysis above indicates that if the transport height of water vapor is different, the dominant microphysical processes will be different. Different dominant microphysical processes caused significant variations in the distribution, intensity, and duration of heavy precipitation during these trials.

4. Discussion and conclusions

A numerical simulation of a heavy rainfall event induced by Super Typhoon Mangkhut (2018) was conducted using the WRF model. The study aimed to investigate the influence of different transport heights of water vapor on the distribution and intensity of heavy precipitation. In the simulation, the water vapor content in the column was kept constant while varying the vertical distribution of water vapor. This allowed for a detailed examination of how changes in the transport height of water vapor impact the characteristics of heavy precipitation. Our main findings are as follows:

The annual mean moisture profile in d03 was compared with the average profile of the heavy precipitation process. Results showed that the average relative humidity during the precipitation process was significantly higher than the annual mean. The difference between the two profiles exhibited two distinct peaks. The first peak was observed in the mid-troposphere, specifically around 600 hPa, while the second peak occurred in the upper troposphere near 200 hPa.

In Trial 2, the moisture profile in d03 was modified to ensure that the vapor mass in each layer maintained the same proportion to the total water vapor mass of the column as the average proportion observed in d03 during September 1981–2010. The results demonstrated a significant variation in the distribution of precipitation compared to the CTRL run. This indicates that altering the transport heights of water vapor can lead to changes in the spatial distribution and intensity of heavy precipitation.

In Trial 3, the water vapor between the two adjacent layers was adjusted to saturation. Results showed that the greatest regional total precipitation occurred when the transport height was at 950–900 hPa, and the lowest when the transport height was at 700–600 hPa. The analysis of the hydrometeor mixing ratios indicates that when the primary transport height was low, liquid-phase processes were dominant. When the transport height was primarily at mid-to-low levels, there would be less convection developing in a more stable environment, which was validated by lower CAPE and $\frac{\partial \theta_e}{\partial z} > 0$. Meanwhile, the aggregation process rather than liquid-phase processes was dominant. When the transport height was primarily at the mid-to-upper levels, deposition and riming processes were the major contributors to heavy precipitation. Microphysical processes in the three trials are summarized in Fig. 14.

Previous investigations of heavy rainfall events have predominantly focused on low-level moisture as a key factor. For instance, Zhang et al. (2020) and Du and Chen (2019) examined atypical Meiyu rainfall and an intense convective precipitation event, respectively, attributing primary importance to low-level moisture transport. Even in studies on rainfall induced by tropical cyclones, such as the work by Shan et al. (2014), low-level moisture has been the main focus. However, Liu et al. (2022) observed high moisture content above 5 km in Typhoon Sinlaku (2020) and emphasized the significance of related thermodynamic processes such as condensation heating. Our study on the precipitation induced by Typhoon Mangkhut (2018) in the Yangtze River Delta region also revealed high relative humidity in the mid-to-upper troposphere, exhibiting a bimodal distribution. The strong moisture transport observed at mid-to-upper levels influenced microphysical processes, consequently impacting precipitation distribution and intensity. These findings are consistent with Zuo et al. (2022), who also stressed the importance of mid-to-upper-level moisture transport.

Our results underscore the influence of moisture transport with high intensities and altitudes by tropical cyclones on microphysical processes, leading to changes in the distribution and intensity of heavy rainfall. This highlights the importance of considering the moisture profile in the vertical direction, particularly at mid-to-upper levels, when predicting rainfall in real cases associated with tropical cyclones. Taking this into account can provide valuable insights for the understanding of precipitation mechanisms during such events.

Author statement

Tianao Liu: methodology, formal analysis, visualization, writing-original draft; Yilun Chen: conceptualization, writing-review & editing, supervision; Shumin Chen: methodology, writing-review & editing; Weibiao Li: funding acquisition; supervision; Aoqi Zhang: methodology, writing-review & editing.

Declaration of competing interest

The authors declare that they have no known competing financial interests or personal relationships that could have appeared to influence the work reported in this paper.

Data availability

Data will be made available on request.

Acknowledgements

This work was supported by the Guangdong Major Project of Basic and Applied Basic Research (Grant No. 2020B0301030004), the National Natural Science Foundation of China (Grant Nos. 42075004, and 42105068, 42005062), and the Innovation Group Project of Southern Marine Science and Engineering Guangdong Laboratory (Zhuhai) (Grant No. 311022006).

Appendix A. Supplementary data

Supplementary data to this article can be found online at https://doi.org/10.1016/j.wace.2023.100587.

References

Ahasan, M.N., Khan, A.Q., 2013. Simulation of a flood producing rainfall event of 29 July 2010 over north-west Pakistan using WRF-ARW model. Nat. Hazards 69 (1), 351–363. https://doi.org/10.1007/s11069-013-0719-6.

Chen, L., 2006. The evolution on research and operational forecasting techniques of tropical cyclones. Journal of Applied Meteorolgical Science 17 (6), 672–681.

Chen, Y., Zhang, A., Zhang, Y., Cui, C., Wan, R., Wang, B., Fu, Y., 2020. A heavy precipitation event in the Yangtze River Basin led by an eastward moving Tibetan plateau cloud system in the summer of 2016. J. Geophys. Res. Atmos. 125 (15) https://doi.org/10.1029/2020JD032429.

Du, Y., Chen, G.X., 2019. Heavy rainfall associated with double low-level jets over southern China. Part II: convection initiation. Mon. Weather Rev. 147 (2), 543–565. https://doi.org/10.1175/mwr-d-18-0102.1.

Evans, J.P., Ekstrom, M., Ji, F., 2012. Evaluating the performance of a WRF physics ensemble over South-East Australia. Clim. Dynam. 39 (6), 1241–1258. https://doi.org/10.1007/s00382-011-1244-5.

Feltz, W.F., Smith, W.L., Howell, H.B., Knuteson, R.O., Woolf, H., Revercomb, H.E., 2003. Near-continuous profiling of temperature, moisture, and atmospheric stability using the atmospheric emitted radiance interferometer (AERI). J. Appl. Meteorol. 42 (5), 584–597. https://doi.org/10.1175/1520-0450(2003)042<0584:Npotma>2.0.Co;2.

Fu, Y., Yu, R., Xu, Y., Xiao, Q., Liu, G., 2003. Analysis on precipitation structures of two heavy rain cases by using TRMM PR and IMI. Acta Meteorol. Sin. 61 (4), 421–431.

Fu, Y.F., Xian, T., Lu, D.R., Liu, G.S., Heng, Z.W., Sun, L., Liu, Q., Wang, Y., Yang, Y.J., 2013. Ozone vertical variations during a typhoon derived from the OMI observations and reanalysis data. Chin. Sci. Bull. 58 (32), 3890–3894. https://doi.org/10.1007/s11434-013-6024-7.

Galarneau, T.J., Bosart, L.F., Schumacher, R.S., 2010. Predecessor rain events ahead of tropical cyclones. Mon. Weather Rev. 138 (8), 3272–3297. https://doi.org/10.1175/2010mwr3243.1.

Gutnick, M., 1962. Mean atmospheric moisture profiles to 31 km for middle latitudes. Appl. Opt. 1 (5), 670–672. https://doi.org/10.1364/AO.1.000670.

Han, B., Du, Y., Wu, C., Liu, X., 2021. Microphysical characteristics of the coexisting frontal and warm-sector heavy rainfall in south China. J. Geophys. Res. Atmos. 126 (21), 24. https://doi.org/10.1029/2021jd035446.

Hersbach, H., Bell, B., Berrisford, P., Hirahara, S., Horányi, A., Muñoz-Sabater, J., Nicolas, J., Peubey, C., Radu, R., Schepers, D., Simmons, A., Soci, C., Abdalla, S., Abellan, X., Balsamo, G., Bechtold, P., Biavati, G., Bidlot, J., Bonavita, M., De Chiara, G., Dahlgren, P., Dee, D., Diamantakis, M., Dragani, R., Flemming, J., Forbes, R., Fuentes, M., Geer, A., Haimberger, L., Healy, S., Hogan, R.J., Hólm, E., Janisková, M., Keeley, S., Laloyaux, P., Lopez, P., Lupu, C., Radnoti, G., de Rosnay, P., Rozum, I., Vamborg, F., Villaume, S., Thépaut, J.N., 2020. The ERA5 global reanalysis. Q. J. R. Meteorol. Soc. 146 (730), 1999–2049. https://doi.org/10.1002/qj.3803.

Hong, S.Y., Noh, Y., Dudhia, J., 2006. A new vertical diffusion package with an explicit treatment of entrainment processes. Mon. Weather Rev. 134 (9), 2318–2341. https://doi.org/10.1175/MWR3199.1.

Hou, A.Y., Kakar, R.K., Neeck, S., Azarbarzin, A.A., Kummerow, C.D., Kojima, M., Oki, R., Nakamura, K., Iguchi, T., 2014. The global precipitation measurement mission. Bull. Am. Meteorol. Soc. 95 (5), 701–722. https://doi.org/10.1175/Bams-D-13-00164.1.

Houze, R.A., 2012. Orographic effects on precipitating clouds. Rev. Geophys. 50, 47. https://doi.org/10.1029/2011rg000365.

Huang, W.R., Chan, J.C.L., Wang, S.Y., 2010. A planetary-scale land-sea breeze circulation in East Asia and the western North Pacific. Q. J. R. Meteorol. Soc. 136 (651), 1543–1553. https://doi.org/10.1002/qj.663.

Huang, Y.J., Wang, Y.P., Xue, L.L., Wei, X.L., Zhang, L.N., Li, H.Y., 2020. Comparison of three microphysics parameterization schemes in the WRF model for an extreme rainfall event in the coastal metropolitan City of Guangzhou, China. Atmos. Res. 240 https://doi.org/10.1016/j.atmosres.2020.104939.

Jiang, J., Qian, Y., Duan, J., Wang, X., Fang, Y., 2022. Numerical simulation of effect of typhoon Mangkhut on extremely heavy rain in Zhejiang Province. J. Trop. Meteorol. 38 (1), 68–80.

Lavers, D.A., Villarini, G., 2015. The relationship between daily European precipitation and measures of atmospheric water vapour transport. Int. J. Climatol. 35 (8), 2187–2192. https://doi.org/10.1002/joc.4119.

Li, J.N., Mai, X.H., Li, F.Z., Mao, J.Y., 2016. Characteristics of the latent heat due to different cloud microphysical processes and their influence on an autumn heavy rain event over hainan island. J. Trop. Meteorol. 22, 57–66. https://doi.org/10.16555/j.1006-8775.2016.S1.006.

Liguori, S., Rico-Ramirez, M.A., Schellart, A.N.A., Saul, A.J., 2012. Using probabilistic radar rainfall nowcasts and NWP forecasts for flow prediction in urban catchments. Atmos. Res. 103, 80–95. https://doi.org/10.1016/j.atmosres.2011.05.004.

Lin, W.S., Xu, S.S., Sui, C.H., 2011. A numerical simulation of the effect of the number concentration of cloud droplets on Typhoon Chanchu. Meteorol. Atmos. Phys. 113 (3–4), 99–108. https://doi.org/10.1007/s00703-011-0152-x.

Lindzen, R.S., 1990. Some coolness concerning global warming. Bull. Am. Meteorol. Soc. 71 (3), 288–299. https://doi.org/10.1175/1520-0477(1990)071<0288:Sccgw>2.0.Co;2.

Liu, L., Han, Y., Xia, Y., Guo, Q., Gao, W., Guo, J., 2022. Investigation of atmospheric dynamic and thermodynamic structures of typhoon Sinlaku (2020) from high-resolution dropsonde and two-way rawinsonde measurements. Rem. Sens. 14 (11) https://doi.org/10.3390/rs14112704.

Lu, X.Q., Yu, H., Ying, M., Zhao, B.K., Zhang, S., Lin, L.M., Bai, L.N., Wan, R.J., 2021. Western North pacific tropical cyclone database created by the China meteorological administration. In: Advances in Atmospheric Sciences. https://doi.org/10.1007/s00376-020-0211-7.

Moore, B.J., Bosart, L.F., Keyser, D., Jurewicz, M.L., 2013. Synoptic-scale environments of predecessor rain events occurring east of the rocky mountains in association with atlantic basin tropical cyclones. Mon. Weather Rev. 141 (3), 1022–1047. https://doi.org/10.1175/Mwr-D-12-00178.1.

Niu, S.J., Jia, X.C., Sang, J.R., Liu, X.L., Lu, C.S., Liu, Y.G., 2010. Distributions of raindrop sizes and fall velocities in a semiarid plateau climate: convective versus stratiform rains. J. Appl. Meteorol. Climatol. 49 (4), 632–645. https://doi.org/10.1175/2009jamc2208.1.

Plotnik, T., Price, C., Saha, J., Guha, A., 2021. Transport of water vapor from tropical cyclones to the upper troposphere. Atmosphere 12 (11). https://doi.org/10.3390/atmos12111506.

Rutledge, S.A., Hobbs, P.V., 1984. The mesoscale and microscale structure and organization of clouds and precipitation in mid-latitude clouds. Part XII : a diagnostic modeling study of precipitation development in narrow cold frontal rainbands. J. Atmos. 41 (20), 2949–2972.

Shan, L., Tan, G., Yao, Y., Wang, Y., 2014. On the water vapor condition and moisture transport for a rain caused by a remote tropical cyclone. J. Trop. Meteorol. 30 (2), 353–360.

Sharma, A., Fernando, H.J.S., Hamlet, A.F., Hellmann, J.J., Barlage, M., Chen, F., 2017. Urban meteorological modeling using WRF: a sensitivity study. Int. J. Climatol. 37 (4), 1885–1900. https://doi.org/10.1002/joc.4819.

Shine, K.P., Sinha, A., 1991. Sensitivity of the Earth's climate to height-dependent changes in the water vapour mixing ratio. Nature 354 (6352), 382–384. https://doi.org/10.1038/354382a0.

Srivastava, P.K., Han, D.W., Rico-Ramirez, M.A., O'Neill, P., Islam, T., Gupta, M., Dai, Q., 2015. Performance evaluation of WRF-Noah Land surface model estimated soil moisture for hydrological application: synergistic evaluation using SMOS retrieved soil moisture. J. Hydrol. 529, 200–212. https://doi.org/10.1016/j.jhydrol.2015.07.041.

Takemi, T., 2007. A sensitivity of squall-line intensity to environmental static stability under various shear and moisture conditions. Atmos. Res. 84 (4), 374–389. https://doi.org/10.1016/j.atmosres.2006.10.001.

Tang, G.Q., Ma, Y.Z., Long, D., Zhong, L.Z., Hong, Y., 2016. Evaluation of GPM Day-1 IMERG and TMPA Version-7 legacy products over Mainland China at multiple spatiotemporal scales. J. Hydrol. 533, 152–167. https://doi.org/10.1016/j.jhydrol.2015.12.008.

Tewari, M., Chen, F., Wang, W., Dudhia, J., LeMone, M.A., Mitchell, K., Ek, M., Gayno, G., Wegiel, J., Cuenca, R.H., 2004. Implementation and verification of the unified Noah land surface model in the WRF model. In: 20th Conference on Weather Analysis and Forecasting/16th Conference on Numerical Weather Prediction.

Tian, J.Y., Liu, J., Yan, D.H., Li, C.Z., Chu, Z.G., Yu, F.L., 2017. An assimilation test of Doppler radar reflectivity and radial velocity from different height layers in improving the WRF rainfall forecasts. Atmos. Res. 198, 132–144. https://doi.org/10.1016/j.atmosres.2017.08.004.

Tian, J.Y., Liu, R.H., Ding, L.Q., Guo, L., Liu, Q., 2021. Evaluation of the WRF physical parameterisations for Typhoon rainstorm simulation in southeast coast of China. Atmos. Res. 247 https://doi.org/10.1016/j.atmosres.2020.105130.

Wang, J., Cui, C., Wang, X., Cui, W., 2014. Analysis on water vapor transport and budget of the severe torrential rain over beijing region on 21 july 2012. Meteorol. Mon. 40 (2), 133–145.

Wang, Y.Q., Wang, Y.Q., Fudeyasu, H., 2009. The role of typhoon songda (2004) in producing distantly located heavy rainfall in Japan. Mon. Weather Rev. 137 (11), 3699–3716. https://doi.org/10.1175/2009mwr2933.1.

Wen, Y.R., Xue, L., Li, Y., Wei, N., Lu, A.M., 2015. Interaction between typhoon Vicente (1208) and the western pacific subtropical high during the beijing extreme rainfall of 21 july 2012. Journal of Meteorological Research 29 (2), 293–304. https://doi.org/10.1007/s13351-015-4097-8.

Wu, L.T., Su, H., Fovell, R.G., Wang, B., Shen, J.T., Kahn, B.H., Hristova-Veleva, S.M., Lambrigtsen, B.H., Fetzer, E.J., Jiang, J.H., 2012. Relationship of environmental relative humidity with North Atlantic tropical cyclone intensity and intensification rate. Geophys. Res. Lett. 39 https://doi.org/10.1029/2012gl053546.

Wu, N., Ding, X., Wen, Z., Chen, G., Meng, Z., Lin, L., Min, J., 2020. Contrasting frontal and warm-sector heavy rainfalls over South China during the early-summer rainy season. Atmos. Res. 235 https://doi.org/10.1016/j.atmosres.2019.104693.

Yan, Z.Y., Ge, X.Y., Guo, B.Y., 2017. Simulated sensitivity of tropical cyclone track to the moisture in an idealized monsoon gyre. Dynam. Atmos. Oceans 80, 173–182. https://doi.org/10.1016/j.dynatmoce.2017.10.008.

Yin, J., Gu, H., Liang, X., Yu, M., Sun, J., Xie, Y., Li, F., Wu, C., 2022. A possible dynamic mechanism for rapid production of the extreme hourly rainfall in zhengzhou city on 20 july 2021. Journal of Meteorological Research 36 (1), 6–25. https://doi.org/10.1007/s13351-022-1166-7.

Ying, M., Zhang, W., Yu, H., Lu, X.Q., Feng, J.X., Fan, Y.X., Zhu, Y.T., Chen, D.Q., 2014. An overview of the China meteorological administration tropical cyclone database. J. Atmos. Ocean. Technol. 31 (2), 287–301. https://doi.org/10.1175/Jtech-D-12-00119.1.

Yu, J.Q., Gao, S., Zhang, L., Shen, X.Y., Guo, L.Y., 2020. Analysis of A Remote rainstorm in the Yangtze River Delta region caused by typhoon Mangkhut (2018). J. Mar. Sci. Eng. 8 (5), 15. https://doi.org/10.3390/jmse8050345.

Yuan, W.H., Yu, R.C., Zhang, M.H., Lin, W.Y., Chen, H.M., Li, J., 2012. Regimes of diurnal variation of summer rainfall over subtropical east asia. J. Clim. 25 (9), 3307–3320. https://doi.org/10.1175/jcli-d-11-00288.1.

Zagrodnik, J.P., McMurdie, L., Conrick, R., 2021. Microphysical enhancement processes within stratiform precipitation on the barrier and sub-barrier scale of the olympic

mountains. Mon. Weather Rev. 149 (2), 503–520. https://doi.org/10.1175/mwr-d-20-0164.1.

Zhang, A.Q., Chen, Y.L., Zhou, S.N., Cui, C.G., Wan, R., Fu, Y.F., 2020. Diurnal variation of Meiyu rainfall in the Yangtze Plain during atypical Meiyu years. J. Geophys. Res. Atmos. 125 (1) https://doi.org/10.1029/2019JD031742.

Zuo, H.S., Chen, Y.L., Chen, S.M., Li, W.B., Zhang, A.Q., 2022. The effect of the water tower of typhoon Mangkhut (2018). Atmosphere 13 (4), 14. https://doi.org/10.3390/atmos13040636.